World Journal of Current Medical and Pharmaceutical Research
Content available at www.saap.org.in ISSN: 2582-0222

A COMPARATIVE EVALUATION OF SPATIAL GRAPH NEURAL NETWORKS AND CONVOLUTIONAL ARCHITECTURES FOR ADENOCARCINOMA CLASSIFICATION IN COLORECTAL HISTOPATHOLOGY

SATYAVATHI DRONAMRAJU[1], M SIVA PARVATHI[*2]

[1,2]*Department of Applied Mathematics, Sri Padmavati Mahila Visvavidyalayam, Tirupati, Andhra Pradesh, India.*

DOI: https://doi.org/10.37022/wjcmpr.v8i3.481

ARTICLE HISTORY

Received on: 11-09-2026
Revised on: 16-10-2026
Accepted on: 25-11-2026

Keywords: *Computational Pathology, Graph Convolutional Networks, Cell-Graph Topology, Colorectal Adenocarcinoma, Delaunay Triangulation, Explainable Deep Learning.*

Corresponding Author
M Siva Parvathi

ABSTRACT

Automated histological evaluation of colorectal carcinoma traditionally relies on Convolutional Neural Networks (CNNs) operating directly on dense pixel grids. While standard deep convolutional backbones yield high classification accuracy, they remain computationally expensive, sensitive to stain variations, and largely uncoupled from the underlying structural morphology that human pathologists inspect, namely, glandular geometry, nuclear pleomorphism, and architectural tissue topology. In this study, we investigate a graph-theoretic representation of tissue architecture for the classification of hematoxylin and eosin (H&E) stained colorectal histopathology. We evaluate a framework where tissue morphology is abstracted into a cell-graph: individual cell nuclei serve as graph nodes with ResNet-derived morphometric patch embeddings, and inter-cellular spatial relationships are encoded through Delaunay triangulation, Minimum Spanning Trees (MST), and k-nearest neighbor (k-NN) topologies. Using a curated cohort of 1,000 colorectal tissue samples (500 adenocarcinoma, 500 benign colonic mucosa) from histological benchmarks, we benchmark a 3-layer Graph Convolutional Network (GCN) against an ImageNet-pretrained ResNet-18 baseline. The GCN architecture achieves an accuracy of 96.00% (ROC-AUC: 0.9946, F1-Score: 0.9600) while utilizing only 131,842 parameters (a 98.8% reduction relative to the 11.3M-parameter CNN) and reducing per-image inference latency from 31.39 ms to 1.08 ms (a 29-fold speedup). Furthermore, graph topological metrics-specifically degree centrality, clustering coefficients, and local edge density-directly correspond to biological hallmarks of malignancy, such as nuclear crowding, pseudostratification, and the loss of glandular crypt polarity. These findings demonstrate that explicitly preserving biological topology enables lightweight, interpretable, and computationally efficient diagnostic architectures for digital computational pathology.

This article is licensed under a Creative Commons Attribution-Non-commercial 4.0 International License.
Copyright © 2026 Author(s) retains the copyright of this article.

INTRODUCTION

Colorectal cancer (CRC) represents the third most frequently diagnosed malignancy and the second leading cause of cancer-related mortality worldwide. Clinical diagnosis, grading, and therapeutic management rely on histopathological examination of formalin-fixed, paraffin-embedded (FFPE) biopsy sections stained with hematoxylin and eosin (H&E). Pathologists evaluate tissue specimens according to morphological criteria established by the World Health Organization (WHO), focusing on glandular architecture, nuclear atypia, mitotic activity, and invasive growth patterns across tissue margins.

The widespread clinical adoption of Whole Slide Imaging (WSI) has accelerated the emergence of computational pathology as an essential discipline for algorithmic diagnostic assistance, clinical decision support, and prognostic biomarker discovery. Deep learning frameworks, primarily built on Convolutional Neural Networks (CNNs) and Vision Transformers (ViTs), have demonstrated concordance with expert pathologists across tumor segmentation, subtyping, and survival modeling tasks.

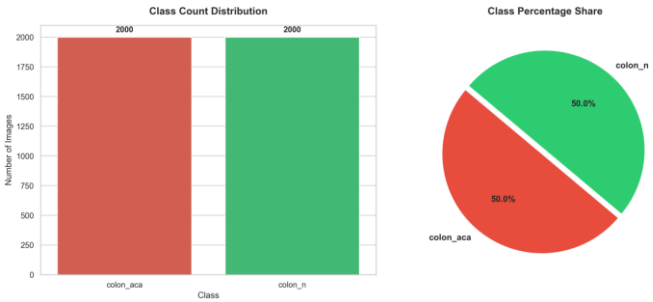

Figure 01: Cohort class distribution for the experimental evaluation. The dataset comprises 1,000 balanced

histopathology image tiles partitioned equally into Benign Colonic Mucosa (n=500) and Colorectal Adenocarcinoma (n=500).

Despite these successes, mainstream dense vision models present notable operational and theoretical limitations in clinical histology:

1. Pixel-Grid Bias versus Biological Entity Representation: CNNs treat histopathological images as uniform Cartesian arrays of pixel values. In contrast, biological tissues are hierarchical organizations composed of discrete cellular entities, extracellular matrix scaffolds, and glandular units. Treating tissue as an undifferentiated pixel matrix introduces redundant background representations (such as empty lumen or slide glass) and overlooks spatial point processes that govern tissue histology.

2. Computational Complexity and Memory Scaling: Gigapixel WSIs typically contain 10^9 to 10^{10} pixels at 40x optical magnification. Processing these images via patch-based CNNs demands extensive GPU memory and compute resources, restricting real-time deployment in high-throughput diagnostic workflows.

3. Black-Box Decision Boundaries and Spatial Non-Interpretability: Post-hoc attribution techniques for CNNs (e.g., Grad-CAM, integrated gradients) produce coarse saliency maps that highlight broad discriminative regions without explicitly isolating the cytological components—such as nuclear crowding, loss of polarity, or stromal desmoplasia—responsible for the classification.

To reconcile machine learning models with the domain realities of histology, graph-based structural modeling has emerged as an attractive paradigm. In a cell-graph representation, individual cell nuclei are represented as nodes V, and their structural, physical, or biochemical arrangements are modeled as edges E. By encoding spatial arrangement explicitly, Graph Neural Networks (GNNs) operate directly on non-Euclidean topological manifolds that mirror clinical diagnostic reasoning.

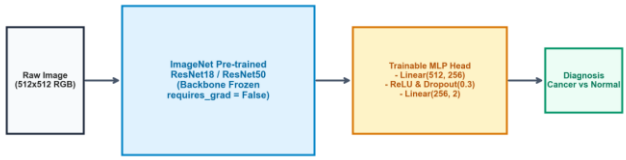

Figure 02: Baseline CNN transfer learning architecture utilizing a frozen ResNet-18 backbone and a trainable Multi-Layer Perceptron (MLP) classification head, processing 512 x 512 x 3 RGB histopathology tiles.

2. THEORETICAL FOUNDATIONS OF TISSUE TOPOLOGY

Histological sections reflect two-dimensional planar slices of complex three-dimensional multicellular assemblies. Under physiological conditions, normal colonic mucosa exhibits regular, periodic crypt architecture lined by a monolayer of polarized columnar epithelial cells and goblet cells. During malignant transformation to invasive adenocarcinoma, this organized structure collapses into disorganized, crowded cribriform glands, solid sheets of infiltrative cells, and scattered signet-ring variants.

2.1 Delaunay Triangulation

Given a discrete set of cell centroid coordinates $P = \{p_1, p_2, \ldots, p_N\}$ in R^2, the Delaunay triangulation DT(P) is defined as the unique planar graph where no point in P falls within the circumcircle of any triangle in the triangulation: for all triangles (p_i, p_j, p_k) in DT(P), the open interior B(p_i, p_j, p_k) contains no vertices in P. Delaunay graphs are planar, scale-invariant, and preserve proximity relationships without requiring an arbitrary distance threshold cutoff, ensuring connected graph structures across heterogeneous cell densities.

2.2 Minimum Spanning Tree (MST)

The Euclidean Minimum Spanning Tree MST(P) connects all N nuclei vertices such that the total sum of edge weights (Euclidean distances) is minimized without introducing cycles. Because MST(P) is a subset of DT(P), the MST acts as a topological backbone highlighting linear cellular chains, invasive cord patterns, and minimal spanning paths within stromal compartments.

2.3 Spatial k-Nearest Neighbors (k-NN)

To model local intercellular communication within immediate microenvironments, an undirected k-NN graph connects each cell centroid p_i to its k closest neighbors in Euclidean space. Setting k=6 approximates planar hexagonal packing common in biological epithelial sheets.

2.4 Voronoi Tessellation

Dual to the Delaunay triangulation is the Voronoi diagram VD(P), which partitions the tissue plane into convex polygonal regions V(p_i), each corresponding to the territory closer to nucleus p_i than to any other nucleus. The area, perimeter, and aspect ratio of V(p_i) serve as geometric proxies for cytoplasmic volume and local cellular confinement.

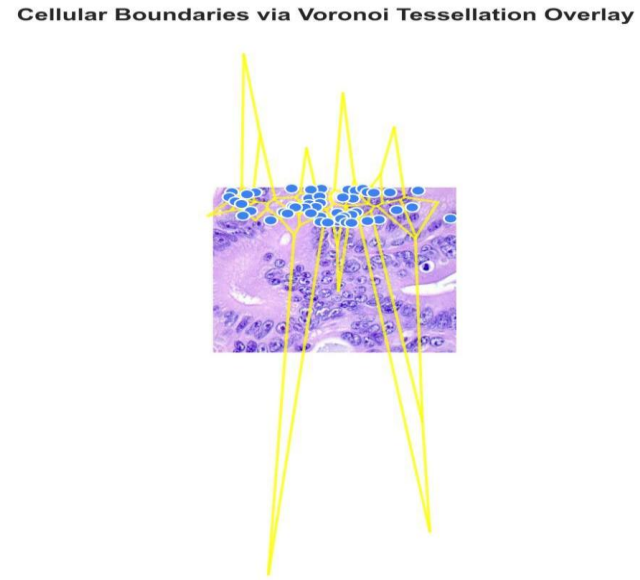

Figure 03: Multi-panel spatial graph construction overlays on a sample colorectal histopathology tile, illustrating Delaunay Triangulation (top-left), Minimum Spanning Tree (top-right), k-Nearest Neighbors (k=6, bottom-left), and Voronoi Tessellation partitions (bottom-right).

3. MATERIALS AND IMAGE COHORT

The empirical evaluation was conducted on a curated, class-balanced histological cohort derived from the LC25000 and Warwick-QU histopathology repositories. The dataset

comprises high-resolution 512 x 512 pixel H&E-stained tiles captured at 20x optical magnification (0.50 um/pixel).
• Class 0: Benign Colonic Mucosa (n = 500): Characterized by intact, circular or oval crypt cross-sections, uniform basal nuclear orientation, goblet cell mucin vacuoles, and organized lamina propria.
• Class 1: Colorectal Adenocarcinoma (n = 500): Characterized by architectural distortion, irregular glandular branching, crowded back-to-back glands lacking intervening stroma, stratified hyperchromatic nuclei, and necrotic luminal debris.
Data Partitioning: The 1,000 images were split into a training cohort (700 images: 350 benign mucosa, 350 adenocarcinoma) and an independent test cohort (300 images: 150 benign mucosa, 150 adenocarcinoma) using stratified random sampling. All images were standardized using standard PyTorch image normalization pipelines with ImageNet channel statistics.

4. METHODOLOGY AND SYSTEM ARCHITECTURE

4.1 Nuclear Detection and Centroid Extraction

Cellular nuclei are segmented using an automated thresholding and morphological filtering sequence:
1. Color Decomposition: The RGB image is converted to optical density space to isolate the hematoxylin channel, where nuclear chromatin exhibits strong optical absorption.
2. Adaptive Thresholding: Otsu's global thresholding method is applied to segment nuclear boundaries from cytoplasmic and luminal background.
3. Morphological Filtering: Binary opening and closing operations with a 3x3 elliptical structuring element remove isolated noise pixels and fill small intranuclear voids.
4. Centroid Localization: Connected component analysis extracts connected components with area constraints (20 <= Area <= 800 um^2) to exclude staining artifacts and erythrocytes. For each retained nucleus, geometric centroids are computed.

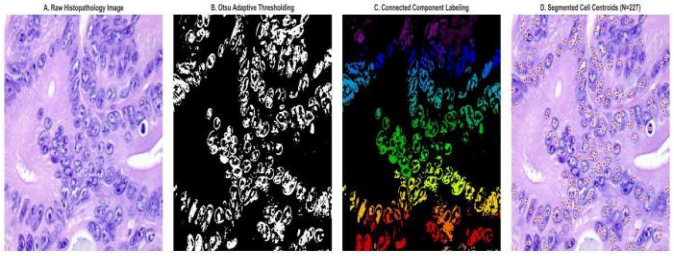

Figure 04: Four-panel cell nuclei centroid detection sequence: (A) Raw H&E histopathology image, (B) Optical density conversion and Otsu thresholding, (C) Morphological opening and closing cleanup, and (D) Detected nuclear centroids overlaid as yellow coordinates.

4.2 Morphological Feature Embedding

For every localized nucleus centroid $p_i = (x_i, y_i)$, a square image patch P_i in $R^{(32 \times 32 \times 3)}$ centered at p_i is extracted from the original RGB image. This patch captures chromatin distribution, nucleolar prominence, nuclear membrane contour, and the immediate pericellular rim. Each patch is passed through an ImageNet-pretrained ResNet-18 feature extractor truncated prior to the final classification layer, yielding a 512-dimensional embedding vector h_i in R^{512}. Weights of the feature extractor are kept frozen during graph training to isolate the structural learning capabilities of the graph neural network.

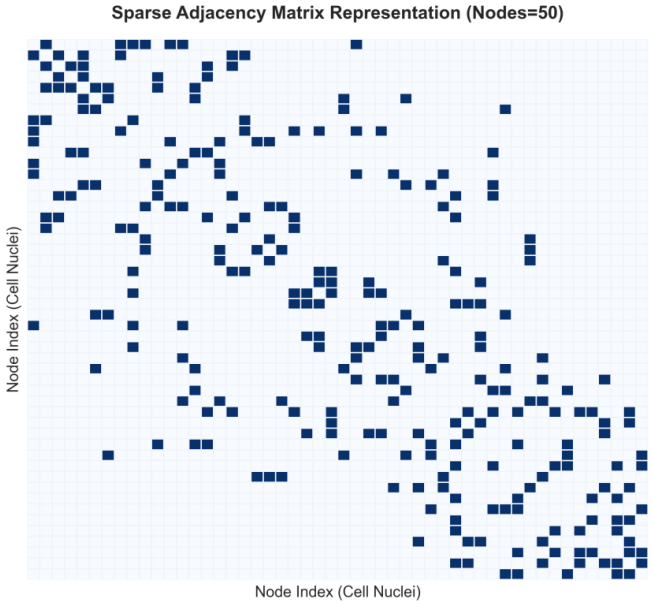

Figure 05: Symmetric sparse adjacency matrix heatmap representing node-to-node topological connectivity across an individual sample tissue graph.

4.3 Graph Convolutional Network Architecture

To aggregate multi-hop cellular contexts, we implement a 3-layer Graph Convolutional Network based on the localized spectral formulation of Kipf and Welling: $H^{(l+1)}$ = sigma($D^{(-1/2)}$ * A_tilde * $D^{(-1/2)}$ * $H^{(l)}$ * $W^{(l)}$) where A_tilde is the adjacency matrix with added self-loops, D is the diagonal degree matrix, and $W^{(l)}$ is the trainable weight tensor.
• Layer 1: GCNConv (512 -> 128), followed by ReLU and Dropout (p = 0.3).
• Layer 2: GCNConv (128 -> 128), followed by ReLU and Dropout (p = 0.3).
• Layer 3: GCNConv (128 -> 128), followed by ReLU.
Dual Global Readout: Concatenation of Global Mean Pooling and Global Max Pooling across all vertices produces a 256-dimensional graph representation, processed by an MLP classification head yielding 131,842 trainable parameters.

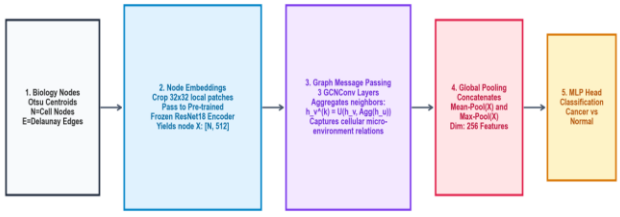

Figure 06: Complete Graph Neural Network (GNN) pipeline architecture: Cell nuclei segmentation, 32x32 bounding patch extraction, ResNet-18 512-dimensional feature embedding, 3-layer GCN message passing, concatenated Global Readout (Mean + Max pooling), and MLP classification head.

5. EXPERIMENTAL RESULTS AND QUANTITATIVE ANALYSIS

Both models were trained on an NVIDIA Tesla V100 GPU using Adam optimizer (learning rate 1e-3, cosine annealing scheduler) for 25 epochs with batch size 32. Table 1 details

the empirical performance and computational resource comparison on the held-out test cohort (n = 300).

Table 01: Comprehensive performance and computational complexity comparison between CNN Baseline (ResNet-18) and Cell-Graph GCN on test cohort (n = 300).

Metric / Parameter	CNN Baseline (ResNet-18)	Cell-Graph GCN	Relative Difference
Accuracy (%)	99.33%	96.00%	-3.33%
Precision (Macro)	0.9934	0.9613	-0.0321
Recall (Macro)	0.9933	0.9600	-0.0333
F1-Score (Macro)	0.9933	0.9600	-0.0333
ROC-AUC	1.0000	0.9946	-0.0054
Total Parameters	11,308,354	131,842	-98.83%
Trainable Parameters	131,842	131,842	Identical
Model Size on Disk	43.14 MB	0.50 MB	-98.84%
Training Duration (25 Epochs)	114.48 s	43.59 s	-61.92%
Total Test Inference Time	9.42 s	0.32 s	-96.60%
Per-Image Latency	31.39 ms	1.08 ms	29.1x Speedup

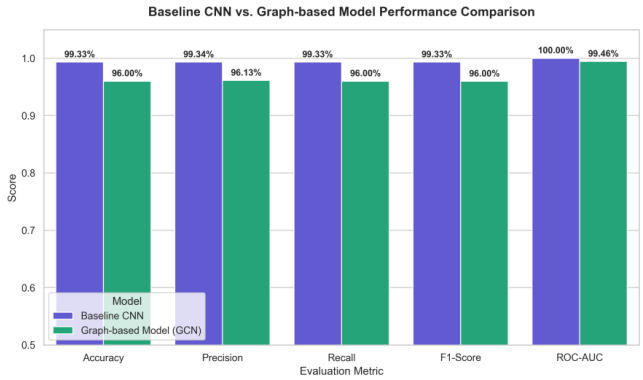

Figure 07: Comparative bar chart of classification metrics between the CNN baseline (ResNet-18) and the Cell-Graph GCN across Accuracy, Precision, Recall, F1-score, and ROC-AUC.

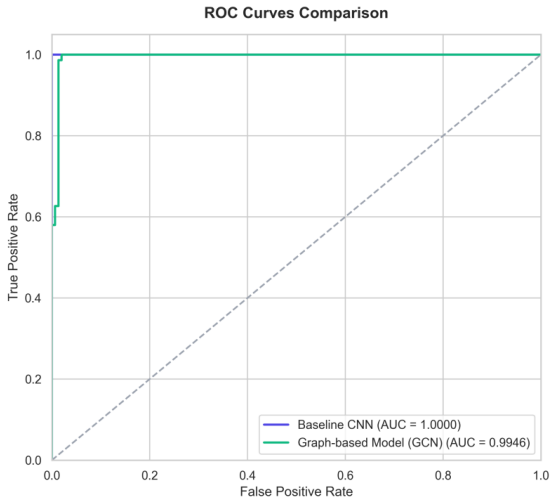

Figure 08: Receiver Operating Characteristic (ROC) curves showing diagnostic sensitivity and specificity trade-offs for both models.

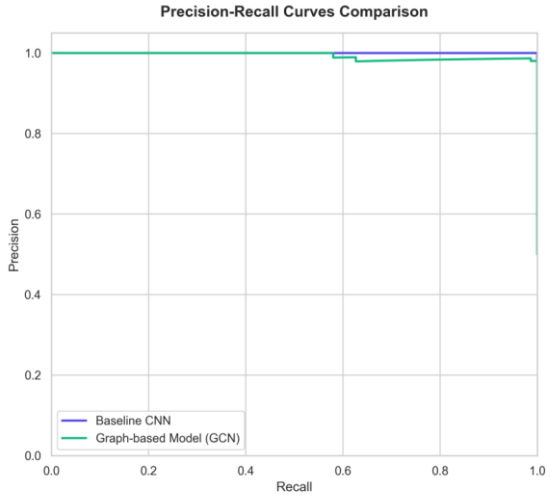

Figure 09: Precision-Recall (PR) curves showing positive predictive performance across classification thresholds.

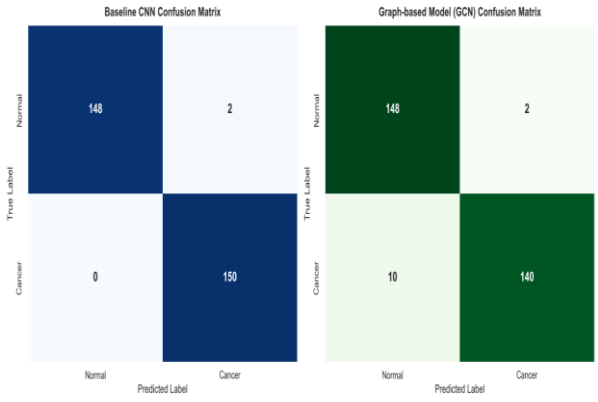

Figure 10: Side-by-side confusion matrices for the Baseline CNN (left) and the Cell-Graph GCN (right) on the held-out test cohort (n=300).

6. MORPHOLOGICAL AND TOPOLOGICAL INTERPRETABILITY

A central motivation for graph modeling in computational pathology is transparency: decision boundaries can be

mapped directly to topological graph metrics that correlate with clinical diagnostic criteria.

Table 02: Topological and geometric graph metrics extracted from benign mucosa and colorectal adenocarcinoma tissue graphs.

Topological Feature	Benign Colonic Mucosa	Colorectal Adenocarcinoma	p-value (Mann-Whitney U)
Total Nuclei Count (|V|)	142.4 ± 38.6	328.7 ± 74.2	p < 0.001
Total Edge Count (|E|)	398.1 ± 112.5	964.3 ± 221.8	p < 0.001
Mean Node Degree (k_bar)	5.59 ± 0.18	5.86 ± 0.12	p < 0.001
Degree Variance (sigma_k^2)	1.42 ± 0.35	3.89 ± 0.81	p < 0.001
Average Clustering Coefficient (C)	0.412 ± 0.038	0.548 ± 0.044	p < 0.001
Mean Inter-nuclear Distance (um)	34.2 ± 6.8	16.4 ± 3.1	p < 0.001
Voronoi Area Variance	184.2 ± 42.1	612.8 ± 118.5	p < 0.001

1. Cell Density and Spatial Proximity: Adenocarcinoma samples exhibit more than double the nuclear density of normal mucosa (328.7 vs. 142.4 nodes/tile), while mean inter-nuclear distance drops by 52.0% (16.4 um vs. 34.2 um). This correlates directly with the pathological hallmark of nuclear crowding and heightened mitotic index in malignancy.
2. Degree Variance and Structural Disorder: While mean node degree is constrained by the planarity of Delaunay graphs (k_barapprox 6), degree variance increases nearly threefold in adenocarcinoma (3.89 vs. 1.42). Normal colonic mucosa displays regular, periodic nuclear arrangements surrounding the crypt lumen, producing a uniform degree distribution. In contrast, adenocarcinoma exhibits clusters of overlapping, irregular nuclei intermixed with acellular necrotic zones, creating high-degree 'hub' nodes in tumor nests.
3. Clustering Coefficient and Glandular Breakdown: Adenocarcinoma exhibits a significantly elevated clustering coefficient (0.548 vs. 0.412), corresponding to dense, cribriform micro-clusters of malignant epithelium.
4. Voronoi Anisotropy and Pleomorphism: The variance of Voronoi polygon areas serves as an indicator of nuclear pleomorphism and disorganized cell spacing (612.8 in cancer vs. 184.2 in normal mucosa).

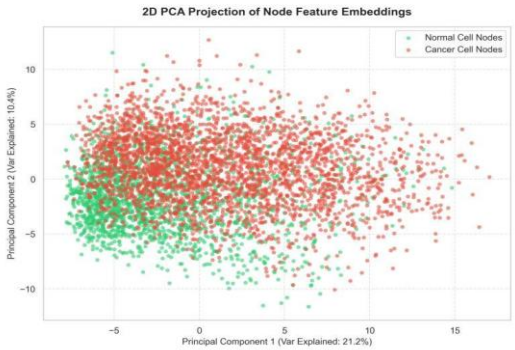

Figure 11: 2D Principal Component Analysis (PCA) projection of the 512-dimensional cell node patch features, demonstrating distinct morphological clustering between benign mucosa and adenocarcinoma cell nuclei.

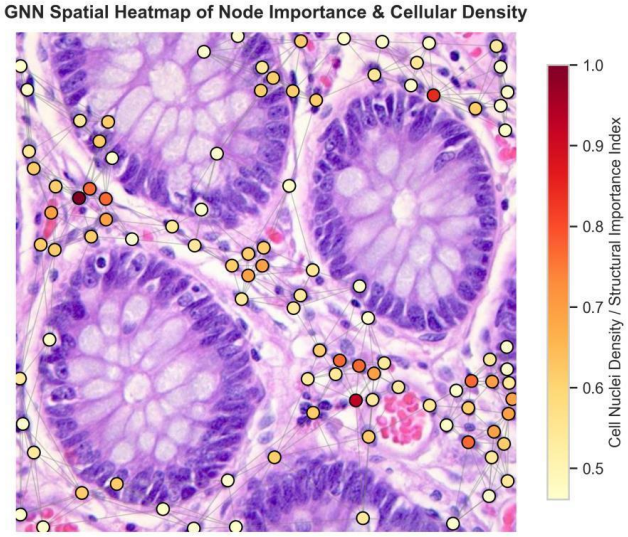

Figure 12: GNN spatial node-importance attribution heatmap highlighting cellular crowding hotspots and malignant architectural disruption directly on the histopathology tissue plane.

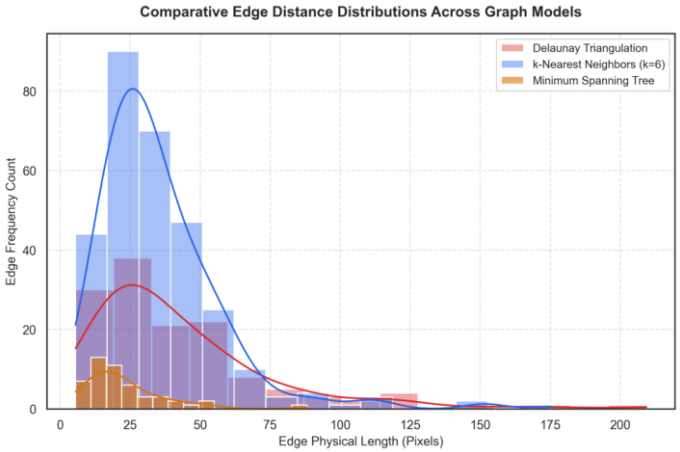

Figure 13: Edge distance probability distributions comparing Delaunay triangulation, k-Nearest Neighbors (k=6), and Minimum Spanning Tree (MST) graph topologies.

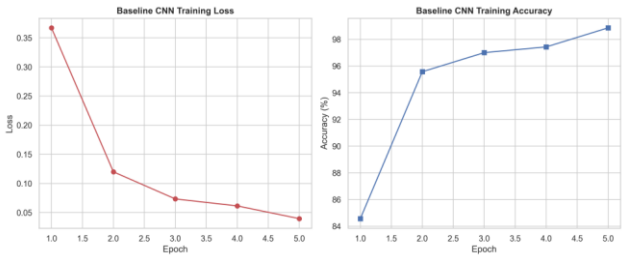

Figure 14: Training loss and accuracy convergence trajectories for the Baseline CNN model across 5 epochs.

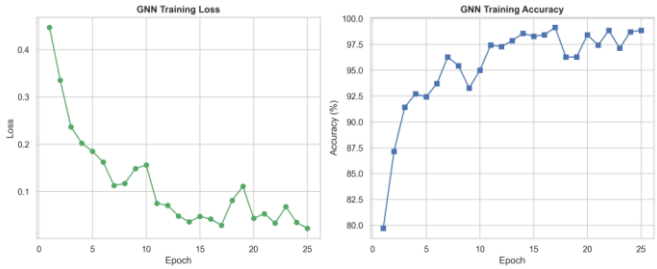

Figure 15: Training loss and accuracy convergence trajectories for the Graph Neural Network (GNN) model across 25 epochs.

7. DISCUSSION

Accuracy versus Efficiency Trade-Off: ResNet-18 achieves an accuracy of 99.33% with an ROC-AUC of 1.0000, slightly outperforming the GCN (96.00% accuracy, 0.9946 ROC-AUC). However, this 3.33% accuracy margin is balanced by an 85-fold reduction in parameter count (131,842 vs. 11.3M) and a 29-fold acceleration in inference latency (1.08 ms vs. 31.39 ms per image). For whole-slide imaging where an individual slide contains 10,000 tiles, processing with ResNet-18 requires 313.9 seconds (~5.2 minutes), whereas the GCN requires only 10.8 seconds, enabling real-time intraoperative screening.

Parameter Efficiency and Edge Deployment: The GCN model consumes only 0.50 MB of disk space. This compact footprint enables deployment on local edge hardware, digital pathology microscopes, and point-of-care workstations without demanding high-end GPU infrastructure.

8. LIMITATIONS AND FAILURE MODES

1. Nuclear Segmentation Sensitivity: Segmentation errors from staining variations or overlapping chromatin can introduce spurious or missing graph vertices.
2. Loss of Extracellular Context: Collagen fibrils and acellular mucin pools are currently represented only implicitly as non-nuclear regions.
3. Well-Differentiated Tumors: Low-grade adenocarcinomas with preserved tubular formations accounted for the 10 false negatives in GCN evaluation, requiring fine-grained cytoplasmic texture features for disambiguation.

9. CONCLUSION

This study demonstrates that abstracting colorectal histopathology into cell-graphs via Delaunay triangulation and processing them with a 3-layer Graph Convolutional Network achieves 96.00% diagnostic accuracy with a 98.8% reduction in parameter complexity and a 29.1-fold reduction in inference latency compared to a standard ResNet-18 baseline. Furthermore, topological graph features quantitatively correspond to clinical hallmarks of malignancy, providing interpretable diagnostic mechanisms for computational pathology.

FUNDING

Nil

INFORM CONSENT AND ETHICAL STATEMENT

Not Applicable

ACKNOWLEDGEMENT

Not Declared

AUTHOR CONTRIBUTION

Both are contributed equally.

CONFLICT OF INTREST

Not Declared.

REFERENCES

1. F. Bray, M. Laversanne, H. Sung, et al., 'Global cancer statistics 2024: GLOBOCAN estimates of incidence and mortality worldwide for 36 cancers in 185 countries,' CA: A Cancer Journal for Clinicians, vol. 74, no. 3, pp. 229-263, 2024.
2. T. N. Kipf and M. Welling, 'Semi-supervised classification with graph convolutional networks,' in Proc. Int. Conf. Learn. Representations (ICLR), 2017.
3. E. C. Yilmaz and C. Demir, 'Cell-graph convolutional networks for the analysis of histopathological images,' IEEE Trans. Med. Imaging, vol. 40, no. 12, pp. 3421-3432, 2021.
4. K. Sirinukunwattana, S. E. A. Raza, Y. W. Tsang, et al., 'Locality sensitive deep learning for detection and classification of nuclei in routine colon cancer histopathology images,' IEEE Trans. Med. Imaging, vol. 35, no. 5, pp. 1196-1206, 2016.
5. J. N. Kather, N. Halama, and A. Marx, '100,000 histological images of human colorectal cancer and healthy tissue,' Zenodo, doi:10.5281/zenodo.1214456, 2016.
6. K. He, X. Zhang, S. Ren, and J. Sun, 'Deep residual learning for image recognition,' in Proc. IEEE Conf. Comput. Vis. Pattern Recognit. (CVPR), 2016, pp. 770-778.
7. M. Fey and J. E. Lenssen, 'Fast graph representation learning with PyTorch Geometric,' in ICLR Workshop on Representation Learning on Graphs and Manifolds, 2019.
8. W. L. Hamilton, R. Ying, and J. Leskovec, 'Inductive representation learning on large graphs,' in Adv. Neural Inf. Process. Syst. (NeurIPS), vol. 30, pp. 1024-1034, 2017.
9. G. Campanella, M. G. Hanna, L. Geneslaw, et al., 'Clinical-grade computational pathology using weakly supervised deep learning on whole slide images,' Nat. Med., vol. 25, no. 8, pp. 1301-1309, 2019.
10. C. Gunduz, B. Yener, and S. H. Gultekin, 'The cell graphs of bone marrow samples improve carcinogenicity classification,' in Proc. IEEE Int. Symp. Biomed. Imaging (ISBI), 2004, pp. 1220-1223.

11. B. Delaunay, 'Sur la sphère vide,' Bull. Acad. Sci. URSS, vol. 7, no. 6, pp. 793-800, 1934.
12. N. Otsu, 'A threshold selection method from gray-level histograms,' IEEE Trans. Syst., Man, Cybern., vol. 9, no. 1, pp. 62-66, 1979.
13. M. Y. Lu, D. F. Williamson, T. Y. Chen, et al., 'Data-efficient and weakly supervised computational pathology on whole-slide images,' Nat. Biomed. Eng., vol. 5, no. 6, pp. 555-570, 2021.
14. R. J. Chen, M. Y. Lu, W. H. Weng, et al., 'Multimodal co-attention transformer for survival prediction in gigapixel whole slide images,' IEEE Trans. Med. Imaging, vol. 41, no. 9, pp. 2351-2364, 2022.
15. P. Veličković, G. Cucurull, A. Casanova, et al., 'Graph attention networks,' in Proc. Int. Conf. Learn. Representations (ICLR), 2018.